Progress In Electromagnetics Research, Vol. 145, 153–161, 2014

The Effect of Antenna Incident Field Distribution on Microwave Tomography Reconstruction

Nozhan Bayat* and Puyan Mojabi

Abstract—For microwave tomography applications, we show that the utilized incident field distribution can affect the achievable image quantitative accuracy and resolution. In particular, for the synthetic cases considered here, it is shown that the use of a focused incident field distribution within the imaging domain often results in either enhanced or equivalent image reconstruction as compared to the use of an omnidirectional incident field distribution.

1. INTRODUCTION

In microwave tomography (MWT), the dielectric profile of the object of interest (OI) is to be found using microwave scattering measurements collected outside the object. To this end, the OI is successively illuminated by a number of antennas located around the OI. The scattering data emanating from the OI is then used by an appropriate nonlinear inversion algorithm so as to generate quantitative images from the dielectric profile of the OI. To make MWT a viable imaging method, specially for clinical applications, its current achievable image quantitative accuracy and resolution need to be enhanced.

Broadly speaking, two general approaches have been suggested to increase the image quantitative accuracy and resolution achievable from MWT: (1) collecting more scattering information, and (2) interpreting the collected scattering information in a better way. Within the framework of these two approaches, some of the utilized techniques are (*i*) increasing the number of antennas (or, probes) [1], (*ii*) using multiple-frequency data sets [2], (*iii*) using different boundary conditions [3], (*iv*) using an appropriate Green's function [4], (*v*) simultaneous use of transverse magnetic and electric data sets [5], (*vi*) using appropriate data calibration techniques [6], (*vii*) using more effective inversion algorithms and regularization techniques [7, 8], (*viii*) accurate MWT system modeling [9], (*ix*) using *a priori* information [10], etc.

Herein, we investigate whether the utilized incident field distribution in MWT, defined as the field distribution within the imaging chamber in the absence of the OI, can affect the achievable image accuracy and resolution. This incident field distribution is usually governed by the near-field distribution of the utilized transmitting antenna as MWT antenna systems usually operate in their near-field zones. It should also be noted that the effect of antenna near-field distribution on the achievable image from microwave radar-based imaging has been studied in [11]; however, to the best of our knowledge, it has not yet been investigated for MWT. (A preliminary investigation of this topic has been presented by the authors as a one-page abstract in [12].) In what follows, we first explain why the choice of the incident field distribution can affect the achievable MWT image accuracy. The numerical model adopted for the incident field distribution will then be described. We will then numerically show how an appropriate choice of the incident field distribution can lead to enhanced image reconstruction.

Received 19 February 2014, Accepted 7 March 2014, Scheduled 12 March 2014

* Corresponding author: Nozhan Bayat (bayatn@myumanitoba.ca).

The authors are with the Electrical and Computer Engineering Department, University of Manitoba, Winnipeg, MB, R3T 5V6, Canada.

2. WHY CAN THE CHOICE OF INCIDENT FIELD DISTRIBUTION AFFECT THE IMAGE ACCURACY?

To understand why the utilized incident field distribution can affect the final image accuracy, let's consider the so-called data equation in MWT:

$$\overbrace{E^{\text{scat}}(\mathbf{p})}^{\text{measured data}} = k_b^2 \int_{\mathcal{D}} \overbrace{g(\mathbf{p},\mathbf{q})E(\mathbf{q})}^{\text{kernel}} \frac{\overbrace{\epsilon(\mathbf{q})}^{\text{unknown}} - \epsilon_b}{\epsilon_b} d\mathbf{q}. \tag{1}$$

In this integral equation, $E^{\text{scat}}(\mathbf{p})$ is the measured scattered field at the receiving point $\mathbf{p}$, which is located outside the imaging domain $\mathcal{D}$. The OI is immersed in a known background medium with a relative complex permittivity of ϵ_b, and the Green's function of $g(\mathbf{p},\mathbf{q})$. The total field, defined as the field distribution within the imaging domain in the presence of the OI, is denoted by $E(\mathbf{q})$. The OI's relative complex permittivity profile, $\epsilon(\mathbf{q})$, is then to be found.

As can be seen from (1), the total field $E(\mathbf{q})$ contributes to the kernel of the data equation integral. In other words, $E(\mathbf{q})$ affects the singular value spectrum of the discretized integral operator [13], characterized by $\mathbf{u}_i$, $\mathbf{v}_i$, and σ_i for the ith left and right singular vectors, and the ith singular value respectively. Therefore, for a given $E(\mathbf{q})$, the discretized unknown permittivity, denoted by the vector $\mathbf{x}$, can be expanded within a subspace of right singular vectors, $\{\mathbf{v}_1, \mathbf{v}_2, \cdots, \mathbf{v}_k\}$ as [13]

$$\mathbf{x} = \sum_{i=1}^{K} \overbrace{\left[\frac{\mathbf{u}_i^H \mathbf{b}}{\sigma_i}\right]}^{\text{weights} \in \mathbb{C}} \mathbf{v}_i \tag{2}$$

where $\mathbf{b}$ is the vector storing the measured data, and the superscript H denotes the Hermitian operator. Due to the ill-posedness of the problem, the above summation is terminated early, say at the index K. (Note that, in general, (2) can be written based on the generalized singular value decomposition [13] which takes into account the effect of regularization terms.).

Based on the above discussion, it can be seen that $E(\mathbf{q})$ contributes to both $\mathbf{v}_i$ and the weights thereof. This is important as (i) appropriate $\mathbf{v}_i$ vectors provide a good basis for the expansion of the unknown permittivity, and (ii) the values of the weights determine the truncation index K. Often, the faster the singular values go to zero, the smaller the truncation index will be. An smaller truncation index means using fewer $\mathbf{v}_i$ vectors to expand the unknown permittivity. Noting that $\mathbf{v}_i$ vectors with large i indices contain high-spatial frequencies [14], the reconstructed permittivity can suffer from limited resolution and accuracy if the above summation is terminated too early. That being said, there might exist an $E(\mathbf{q})$ that results in optimized singular value dynamics for this problem. One indication for such an $E(\mathbf{q})$ will be the one that maximizes the number of significant singular values of the discretized integral equation.

The above discussion speculated that with an appropriate $E(\mathbf{q})$ enhanced reconstruction might be obtained. Now, the question to be answered is: *what tools do we have to control $E(\mathbf{q})$ within the imaging domain?* It is known that, for a given MWT configuration (i.e., a system with a fixed known Green's function), $E(\mathbf{q})$ depends on both $\epsilon(\mathbf{q})$ and the incident field distribution $E^{\text{inc}}(\mathbf{q})$. However, noting that $\epsilon(\mathbf{q})$ is the unknown of the problem, it cannot be used to control the total field distribution. For the same reason, we can never completely control the total field distribution within the imaging domain. However, with changing $E^{\text{inc}}(\mathbf{q})$, we can, to some extent, affect and change $E(\mathbf{q})$ within the imaging domain; thus, affecting the final MWT image. This completes our discussion on the possibility of using the incident field distribution toward achieving an enhanced MWT image. In the rest of this letter, we attempt to numerically demonstrate this idea.

3. NUMERICAL MODEL FOR INCIDENT FIELD DISTRIBUTION

As discussed above, the achievable image accuracy can be affected by changing the incident field distribution within the imaging domain. To demonstrate this for a 2D transverse magnetic (TM_z) problem, we consider the following model for the incident field distribution (similar to that used in [15])

$$\boldsymbol{E}^{\text{inc}}(x,y) = \hat{z} C H_0^2(k_b \rho) \cos^m \psi \tag{3}$$

where C is a constant, (x, y) the observation point within the imaging domain, and $H_0^2(\cdot)$ the zeroth-order Hankel function of the second kind. The distance from the transmitting antenna to the observation point is denoted by ρ. The angle ψ is the angle between the antenna boresight axis and the line connecting the antenna to the observation point. The non-negative variable m represents the focusing level of the incident field distribution: the larger m, the more focused the incident field distribution. Also, as can be seen in (3), $m = 0$ represents an omni-directional incident field distribution (i.e., the incident field due to a line source).

It should be noted that the practical implementation of such focused incident field distribution is not within the scope of this paper. However, we envision three different methods to achieve such focused near-field distribution. The first method relies on using antenna array techniques. This can be practical as MWT setups usually utilize co-resident antenna elements ranging from 16 to 64 antennas [7, 16–19] placed in an imaging chamber. Currently, these antennas are being used individually for illuminating the OI. Therefore, there is an opportunity to collectively use all these antenna elements to create sufficient number of appropriate incident field distributions. This can be pursued by proper simultaneous excitation of these co-resident antenna elements using antenna array techniques. The second method relies on modification of the individual antenna element to achieve a focused near-field distribution. Within this framework, the use of microwave near-field plates, whose ability to achieve focusing in near-field has been recently demonstrated [20], seems very promising. Also, the use of appropriate modifications such as incorporating a dielectric director [21] into the individual antenna element is another possibility. The third method could be simply based on the combination of the previous two methods.

4. RECONSTRUCTION RESULTS

Three different OIs are considered. For a given OI, we collect several scattering data sets, each of which corresponds to utilizing an incident field distribution with a certain focusing level. (3% white noise is added to all data sets according to [22].) Each of these data sets will then be separately inverted. The utilized incident field distribution in the inversion algorithm will be the same incident field distribution that has been used to collect that scattering data set. Specifically, Sections 4.1 and 4.3 use the multiplicative-regularized Gauss-Newton inversion (MR-GNI) algorithm [23, 24] to invert the data sets. Section 4.2, on the other hand, deals with shape and location reconstruction using the binary implementation of the MR-GNI algorithm as presented in [25].

4.1. Resolution Test

We consider two lossless circular objects with the radius of 20.5 mm and the relative permittivity of $\epsilon_r = 4$ at the frequency of operation $f = 3$ GHz which are separated by 15 mm, as shown in Figure 1(a). In the first configuration, this target will be successively illuminated by 8 antennas equally distributed on a circle of radius 0.1 m. (Total number of data points will then be 8×7 data points; due to reciprocity, half of which will be redundant.) For this configuration, we collect three different data sets, each of which corresponds to using a certain focusing level for the utilized incident field distribution; namely, $m = 0, 30, 70$. The inversion results for this configuration are shown in Figures 1(b)–(d). It can be seen that (i) these inversion results are different, and (ii) the reconstructed permittivity is more accurate and exhibit enhanced resolution when $m = 70$. In the second configuration, we repeat the previous experiment while having 24 antennas; thus, having 24×23 data points. The reconstruction results corresponding to the two extreme cases ($m = 0, 70$) are shown in Figure 2. This example clearly shows that the use of different incident field distributions can result in images with different accuracies.

We speculate that by making the incident field distribution more focused within the imaging domain, the kernel of (1) becomes less smooth; thus, making the problem less ill-posed [13, Section 2.2], and consequently improving the final image. This can be better seen by comparing the singular values of the Jacobian (sensitivity) matrix for different values of m at the last iteration of the MR-GNI algorithm as shown in Figure 3: the singular values corresponding to $m = 70$ are larger than those corresponding to smaller m values. We have also tried this example when the transmitters are located on a circle of radius 1 m (i.e., 10λ at the frequency of operation). In this configuration, the reconstruction results for these different m values were almost identical. Noting that the imaging domain in this configuration is located in the far-field zone of the transmitting antennas, these different m values do not significantly change the incident field distribution within the imaging domain; thus, resulting in no considerable changes in the reconstruction results.

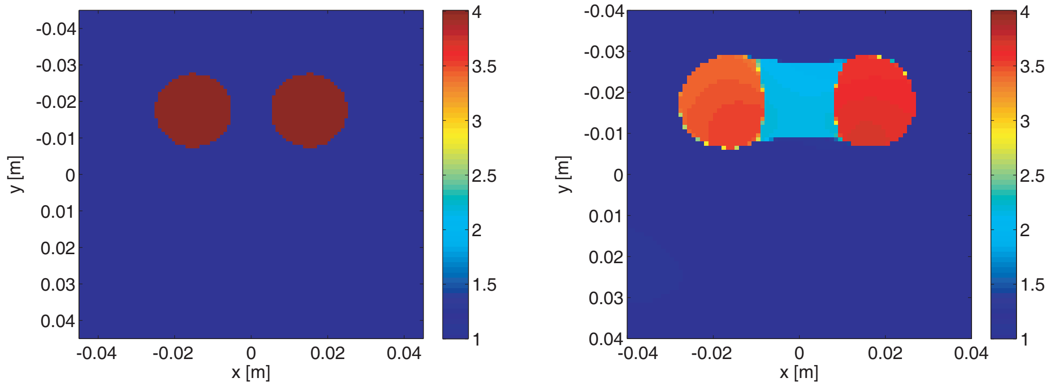

(a) True Re(ϵ_r) (b) Re(ϵ_r), $m = 0$

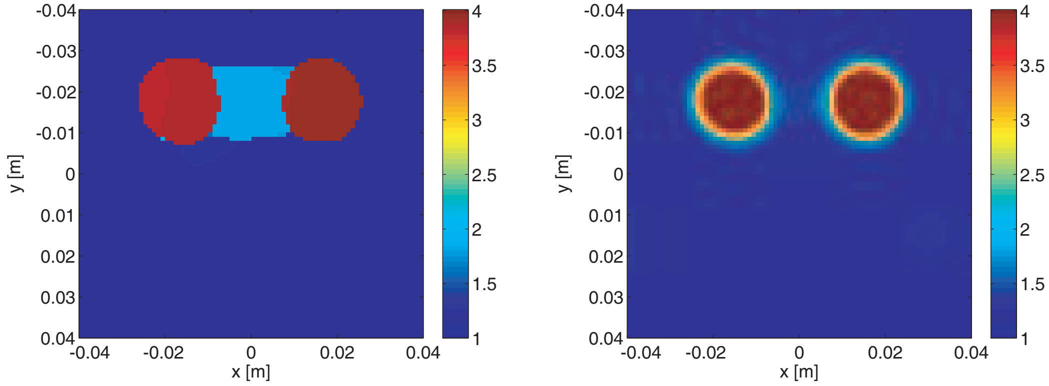

(c) Re(ϵ_r), $m = 30$ (d) Re(ϵ_r), $m = 70$

Figure 1. Resolution test using 8 antennas: (a) true dielectric profile (The zero imaginary part of the permittivity is not shown.); (b)–(d) reconstructed dielectric profile using three different focusing levels (m) for the utilized incident field distribution.

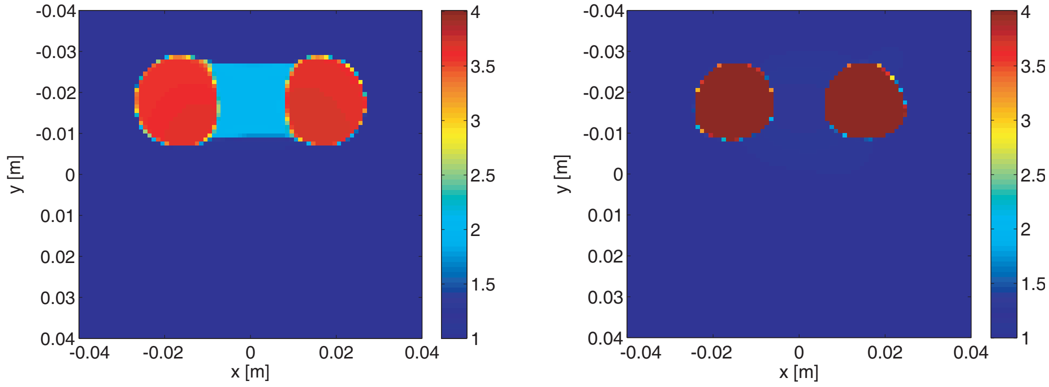

(a) Re(ϵ_r), $m = 0$ (b) Re(ϵ_r), $m = 70$

Figure 2. Resolution test using 24 antennas: reconstructed dielectric profile using two different focusing levels for the utilized incident field distribution.

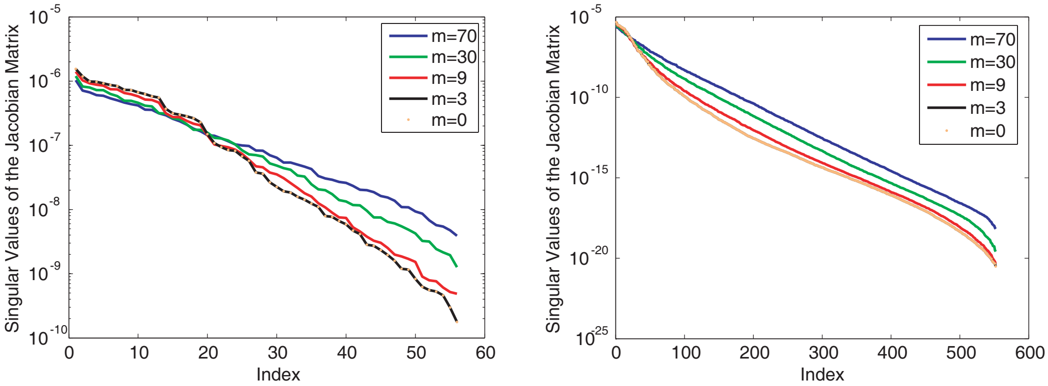

(a) 8 antennas (b) 24 antennas

Figure 3. Resolution test using 8 and 24 antennas: singular values of the Jacobian matrix at the last MR-GNI iteration for different m values.

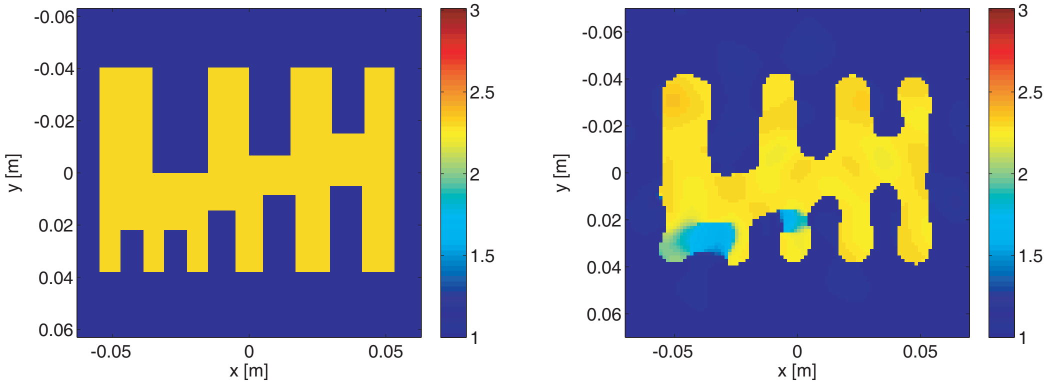

(a) True Re(ϵ_r) (b) $m = 0$

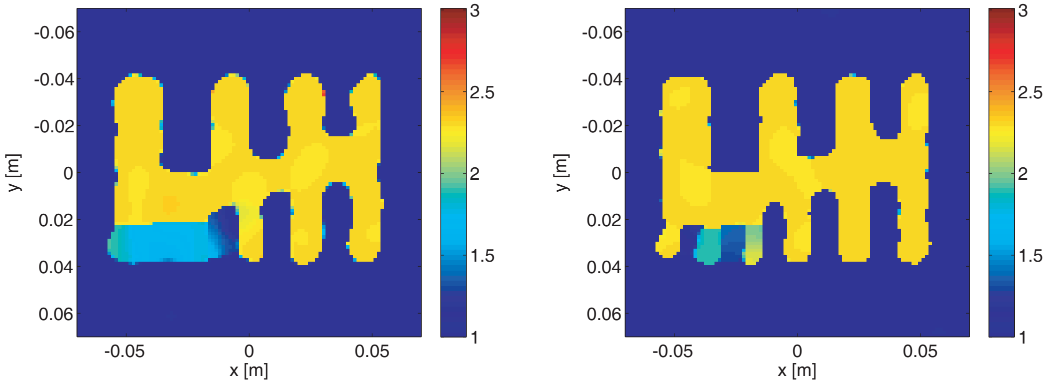

(c) $m = 70$ (d) $m = 300$

Figure 4. Concentric squares test case: (a)–(b) true dielectric profile; reconstructed dielectric profile when (c)–(d) $m = 0$, and (e)–(f) $m = 70$.

4.2. E-Shape Object

We consider the so-called Semenov's E-shape object [17], as shown in Figure 4(a). This object is chosen to be lossless with the relative permittivity of 2.3. This object is illuminated with 16 antennas (thus, having 16 × 15 data points), located on a circle with the radius of 0.15 m with three different focusing levels: $m = 0$, 70, and 300. We then use the binary implementation of the MR-GNI algorithm [25] to invert these data sets. As shown in Figures 4(b)–(c), the reconstruction results for $m = 0$ and $m = 70$ are not capable of reconstructing the three small fingers located at the bottom left part of the object. However, with $m = 300$, the inversion algorithm is capable of capturing these three fingers. The singular values of the Jacobian matrix in the last iteration of the inversion algorithm for different m values are shown in Figure 6(a). As can be seen, the singular values corresponding to $m = 300$ decay more slowly as compared to those for $m = 0$ and 70.

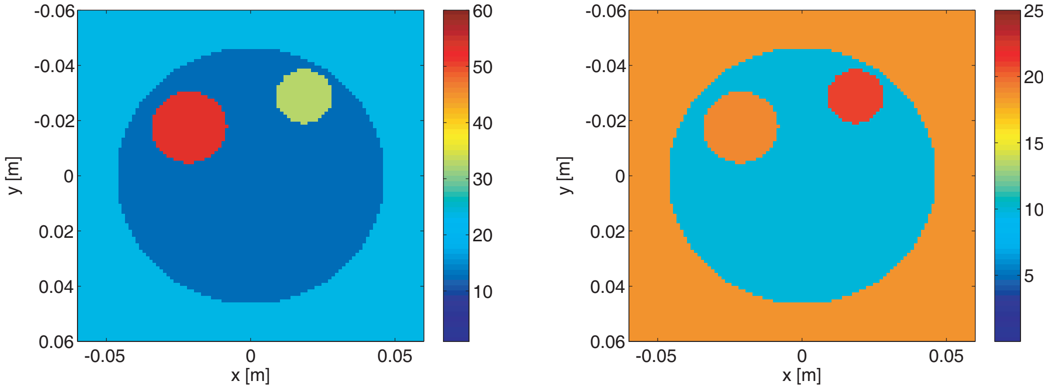

(a) True Re(ϵ_r) (b) True Im(ϵ_r)

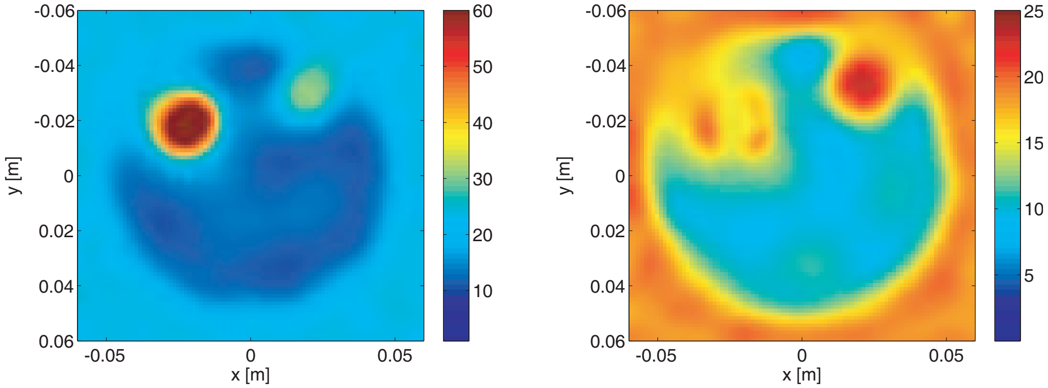

(c) Re(ϵ_r), $m = 0$ (d) Im(ϵ_r), $m = 0$

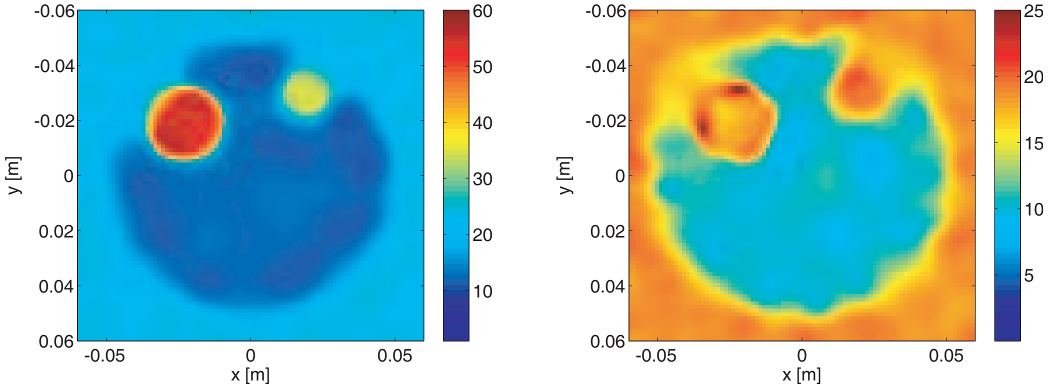

(e) Re(ϵ_r), $m = 70$ (f) Im(ϵ_r), $m = 70$

Figure 5. Breast test case using 24 antennas: (a)–(b) true dielectric profile; reconstructed dielectric profile when (c)–(d) $m = 0$, and (e)–(f) $m = 70$.

4.3. Breast Model

In this example, we use a breast model that has been previously used in [3, 16]. As shown in Figures 5(a)–(b), this model consists of three regions: fibroglandular (smallest circle), tumor (medium circle), and fatty (largest circle) tissues. The background medium is chosen to be $23.4 + j18.5$ at the frequency of operation, which is 1 GHz (similar to the background medium used for the breast cancer microwave imaging system at Dartmouth College [16]). This numerical model is illuminated by 24 antennas, which are located on a circle of radius 0.1 m. The inversion results for $m = 0,\ 70$ are shown in Figures 5(c)–(f). As can be seen, the reconstructed image when $m = 70$ is more accurate than the reconstructed image when $m = 0$. Specifically, the true tumor permittivity is $53.4 + j18.8$, whereas the reconstructed tumor permittivity at the center of inclusion is $63.4 + j15.4$ when $m = 0$, and is $53.7 + j17.7$ when $m = 70$. As shown in Figure 6(b), the singular values of the Jacobian matrix at the last MR-GNI iteration when $m = 70$ are larger than those when $m = 0$. We also attempted to reconstruct this profile using only 4 antennas; however, reconstruction was not successful for any m values that we tried. When using 4 antennas, we noticed that the singular values of the Jacobian (sensitivity) matrix at the last MR-GNI iteration when $m = 0$ were larger than those when $m = 70$. This observation is not consistent with what we observed in earlier examples. This inconsistency might be justified as follows. If only 4 antennas with focused near-field distribution ($m = 70$) are used, we cannot sufficiently illuminate every part within the imaging domain; thus, losing sensitivity to some imaging areas. On the other hand, if 4 antennas with omnidirectional field distribution ($m = 0$) are used, it is more likely to illuminate everywhere within the imaging domain sufficiently; thus, enhancing the sensitivity compared to the use of few focused beams.

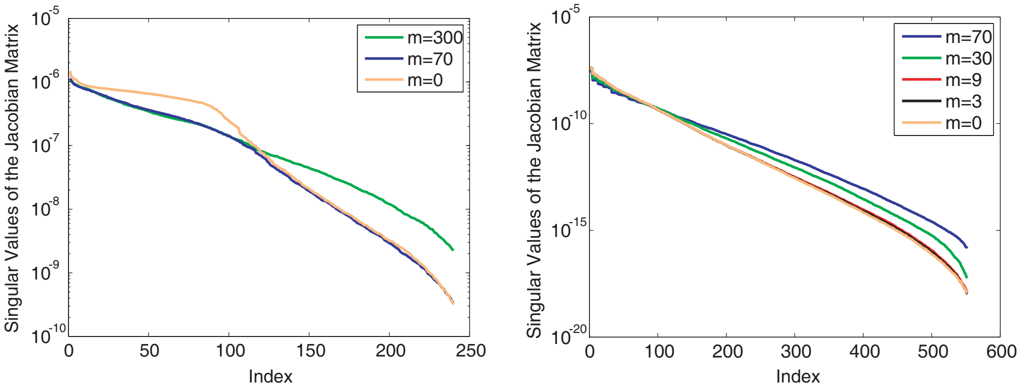

(a) E-shape object (b) Breast model

Figure 6. Singular values of the Jacobian matrix at the last MR-GNI iteration for different m values for the last two targets.

5. CONCLUSION

We have shown that the choice of the incident field distribution can affect the achievable image quantitative accuracy and resolution. For all the results shown here, the use of a focused incident field distribution improved image accuracy and resolution. However, it should be noted that we have also experienced no imaging improvements with the use of focused incident field distribution (not shown here). Therefore, this paper demonstrates the idea that the proper choice of the incident field can improve the image accuracy. This adds one more parameter to be optimized in the design of an MWT system. Future work should address the conditions under which this improvement will occur as well as the practical implementation of this idea.

ACKNOWLEDGMENT

The authors would like to thank the Natural Sciences and Engineering Research Council (NSERC) of Canada, and University of Manitoba Research Grant Program for their financial support.

REFERENCES

1. Ostadrahimi, M., P. Mojabi, S. Noghanian, J. LoVetri, and L. Shafai, "A multiprobe-per-collector modulated scatterer technique for microwave tomography," *IEEE Antennas Wireless Propag. Lett.*, Vol. 10, 1445–1448, 2011.
2. Shea, J. D., P. Kosmas, S. C. Hagness, and B. D. V. Veen, "Three-dimensional microwave imaging of realistic numerical breast phantoms via a multiple-frequency inverse scattering technique," *Medical Physics*, Vol. 37, No. 8, 4210–4226, 2010.
3. Mojabi, P. and J. LoVetri, "A novel microwave tomography system using a rotatable conductive enclosure," *IEEE Trans. Antennas Propag.*, Vol. 59, No. 5, 1597–1605, 2011.
4. Okhmatovski, V., J. Aronsson, and L. Shafai, "A well-conditioned non-iterative approach to solution of the inverse problem," *IEEE Trans. Antennas Propag.*, Vol. 60, No. 5, 2418–2430, 2012.
5. Abubakar, A., T. M. Habashy, and P. M. Van den Berg, "Nonlinear inversion of multi-frequency microwave Fresnel data using the multiplicative regularized contrast source inversion," *Progress In Electromagnetics Research*, Vol. 62, 193–201, 2006.
6. Ostadrahimi, M., P. Mojabi, C. Gilmore, A. Zakaria, S. Noghanian, S. Pistorius, and J. LoVetri, "Analysis of incident field modeling and incident/scattered field calibration techniques in microwave tomography," *IEEE Antennas Wireless Propag. Lett.,* Vol. 10, 900–903, 2011.
7. Abubakar, A., P. M. Van den Berg, and S. Y. Semenov, "Two- and three-dimensional algorithms for microwave imaging and inverse scattering," *Journal of Electromagnetic Waves and Applications*, Vol. 17, No. 2, 209–231, 2003.
8. Habashy, T. M. and A. Abubakar, "A general framework for constraint minimization for the inversion of electromagnetic measurements," *Progress In Electromagnetics Research*, Vol. 46, 265–312, 2004.
9. Meaney, P., K. Paulsen, J. Chang, M. Fanning, and A. Hartov, "Nonactive antenna compensation for fixed-array microwave imaging. II. Imaging results," *IEEE Trans. Med. Imag.*, Vol. 18, No. 6, 508–518, 1999.
10. Gilmore, C., A. Abubakar, W. Hu, T. Habashy, and P. Van den Berg, "Microwave biomedical data inversion using the finite-difference contrast source inversion method," *IEEE Trans. Antennas Propag.*, Vol. 57, No. 5, 1528–1538, 2009.
11. Bourqui, J., M. Campbell, T. Williams, and E. Fear, "Antenna evaluation for ultra-wideband microwave imaging," *International Journal of Antennas and Propagation*, Vol. 2010, 2010.
12. Bayat, N. and P. Mojabi, "On the effect of antenna illumination patterns on the accuracy and resolution of microwave tomography," *IEEE APS/URSI*, Jul. 2013.
13. P. C. Hansen, "Numerical tools for analysis and solution of Fredholm integral equations of the first kind," *Inverse Probl.*, Vol. 8, No. 6, 849, 1992.
14. P. C. Hansen, M. E. Kilmer, and R. H. Kjeldsen, "Exploiting residual information in the parameter choice for discrete ill-posed problems," *BIT Numerical Mathematics*, Vol. 46, No. 1, 41–59, 2006.
15. F. Caramanica and G. Oliveri, "An innovative multi-source strategy for enhancing the reconstruction capabilities of inverse scattering techniques," *Progress In Electromagnetics Research*, Vol. 101, 349–374, 2010.
16. Rubæk, T., P. M. Meaney, P. Meincke, and K. D. Paulsen, "Nonlinear microwave imaging for breast-cancer screening using Gauss-Newton's method and the CGLS inversion algorithm," *IEEE Trans. Antennas Propag.*, Vol. 55, No. 8, 2320–2331, Aug. 2007.
17. Semenov, S., R. Svenson, A. Bulyshev, A. Souvorov, A. Nazarov, Y. Sizov, V. Posukh, A. Pavlovsky, P. Repin, and G. Tatsis, "Spatial resolution of microwave tomography for detection of myocardial ischemia and infarction-experimental study on two-dimensional models," *IEEE Trans. Microwave Theory Tech.*, Vol. 48, No. 4, 538–544, Apr. 2000.
18. Gilmore, C., P. Mojabi, A. Zakaria, M. Ostadrahimi, C. Kaye, S. Noghanian, L. Shafai, S. Pistorius, and J. LoVetri, "A wideband microwave tomography system with a novel frequency selection procedure," *IEEE Transactions on Biomedical Engineering*, Vol. 57, No. 4, 894–904, Apr. 2010.

19. Abubakar, A., P. M. Van den Berg, and J. J. Mallorqui, “Imaging of biomedical data using a multiplicative regularized contrast source inversion method,” *IEEE Trans. Microwave Theory Tech.*, Vol. 50, No. 7, 1761–1777, Jul. 2002.
20. Grbic, A., L. Jiang, and R. Merlin, “Near-field plates: Subdiffraction focusing with patterned surfaces,” *Science*, Vol. 320, No. 5875, 511–513, Apr. 2008.
21. Bourqui, J., M. Okoniewski, and E. Fear, “Balanced antipodal Vivaldi antenna with dielectric director for near-field microwave imaging,” *IEEE Trans. Antennas Propag.*, Vol. 58, No. 7, 2318–2326, Jul. 2010.
22. Abubakar, A., P. M. Van den Berg, and S. Y. Semenov, “A robust iterative method for born inversion,” *IEEE Trans. Geosci. Remote Sensing*, Vol. 42, No. 2, 342–354, Feb. 2004.
23. Abubakar, A., T. M. Habashy, V. L. Druskin, L. Knizhnerman, and D. Alumbaugh, “2.5D forward and inverse modeling for interpreting low-frequency electromagnetic measurements,” *Geophysics*, Vol. 73, No. 4, F165–F177, Jul.–Aug. 2008.
24. Mojabi, P. and J. LoVetri, “Microwave biomedical imaging using the multiplicative regularized Gauss-Newton inversion,” *IEEE Antennas Wireless Propag. Lett.*, Vol. 8, 645–648, 2009.
25. Mojabi, P., J. LoVetri, and L. Shafai, “A multiplicative regularized Gauss-Newton inversion for shape and location reconstruction,” *IEEE Trans. Antennas Propag.*, Vol. 59, No. 12, 4790–4802, 2011.